

The tuning of para- and diamagnetic cavity photon excitations in a square array of quantum dots in a magnetic field

Vidar Gudmundsson,^{1,*} Vram Mughnetsyan,^{2,†} Hsi-Sheng Goan,^{3,4,5,‡} Jeng-Da Chai,^{3,4,5,§} Nzar Rauf Abdullah,^{6,¶} Chi-Shung Tang,^{7,**} Valeriu Moldoveanu,^{8,††} and Andrei Manolescu^{9,‡‡}

¹*Science Institute, University of Iceland, Dunhaga 3, IS-107 Reykjavik, Iceland*

²*Department of Solid State Physics, Yerevan State University, Alex Manoogian 1, 0025 Yerevan, Armenia*

³*Department of Physics and Center for Theoretical Physics,
National Taiwan University, Taipei 106319, Taiwan*

⁴*Center for Quantum Science and Engineering, National Taiwan University, Taipei 106319, Taiwan*

⁵*Physics Division, National Center for Theoretical Sciences, Taipei 106319, Taiwan*

⁶*Physics Department, College of Science, University of Sulaimani, Kurdistan Region, Iraq*

⁷*Department of Mechanical Engineering, National United University, Miaoli 36003, Taiwan*

⁸*National Institute of Materials Physics, PO Box MG-7, Bucharest-Magurele, Romania*

⁹*Department of Engineering, Reykjavik University, Menntavegur 1, IS-102 Reykjavik, Iceland*

We employ a “real-time” excitation scheme to calculate the excitation spectra of a two-dimensional electron system in a square array of quantum dots placed in a circular cylindrical far-infrared photon cavity subjected to a perpendicular homogeneous external magnetic field. The Coulomb interaction of the electrons is handled via spin density functional theory and the para- and the diamagnetic parts of the electron-photon coupling are updated according to a configuration interaction method in each iteration of the density functional calculation. The results show that an excitation scheme built on using the symmetry of the lateral square superlattice of the dots and the cylindrical cavity produces both para- and diamagnetic resonance peaks with oscillator strengths that can be steered by the excitation pulse parameters. The excitation method breaks the conditions for the generalized Kohn theorem and allows for insight into the subband structure of the electron system and can be used both in and outside the linear response regime.

I. INTRODUCTION

Far-infrared (FIR) spectroscopy of various types has the last four decades been important to study carrier excitations in the conduction band of two-dimensional electron systems, homogeneous or modulated. The extraordinary purity and mobility of the two-dimensional electron gas (2DEG) in GaAs and related heterostructures has been instrumental in establishing bounds on theoretical models and aid in their development [1–5].

Early on, it was realized that FIR spectroscopy has its limitations set by general symmetry arguments, most notable being the original Kohn theorem stating that the cyclotron resonance is not influenced by the Coulomb interaction as long as the exciting electrical field can be viewed as a homogeneous rotating microwave field and the kinetic term for the electrons is quadratic in the momentum [6]. Later on, this was expanded to the so-called generalized Kohn theorem stating that the FIR excitation of parabolically confined electrons in quantum dots and wires can only excite their center of mass (CM) motion if the wavelength of the exciting electrical field is

much longer than the characterized length of the electronic system [7, 8]. Even though the Kohn theorems tend to “block the view” of the internal dynamics of the particular electron systems, they play an important role as tests on the accuracy of analytical and numerical models. Moreover, their prerequisites are not always totally fulfilled for experimental systems, so many deviations from them are known. For example, the confinement is not always parabolic [9–12], with Raman scattering a finite wavevector is imposed on the system [13, 14], the kinetic energy in GaAs can be slightly non-parabolic for higher order processes [15], and in graphene and graphene-like systems the kinetic energy is linear in the momentum operator [16].

The successful placement of extended 2DEGs in FIR photon cavities and external homogeneous magnetic field opens up further avenues to explore their properties and has instigated researchers to examine the regime of non-perturbative electron-light coupling [17, 18]. Concurrently, to the experimental development, several directions have been taken in the theoretical modeling of extended or localized electron systems in microcavities [19, 20], or atomic systems in chemistry [21–23], under the general name of quantum electrodynamical density functional theory (QEDFT). Here, we will follow the general outlines of Malave *et. al.* under the acronym of QEDFT-TP, where TP stands for the tensor product of the electron and the photon states used in their approach [24].

Parallel to this development, research groups are working on cavity quantum materials of various types [25]. In

* vidar@hi.is

† vram@ysu.am

‡ goan@phys.ntu.edu.tw

§ jdchai@phys.ntu.edu.tw

¶ nzar.r.abdullah@gmail.com

** cstang@nuu.edu.tw

†† valim@infim.ro

‡‡ manoles@ru.is

this work we present numerical calculations which show how a specially designed FIR-photon cavity and a time-dependent excitation can be used to shed light on the internal dynamics of the electrons in the 2DEG-cavity system, and how it is possible to select the type of the underlying processes determining the characteristics of an excited state of the system.

In continuation of the previous modeling of the static state of a 2DEG in an array of quantum dots in an external magnetic field placed in a cylindrical FIR-cavity [26], we show how time-dependent excitation of the system can be implemented in order to emphasize magnetically active photon processes controlling the ratio of virtual and real para- and diamagnetic transitions to reach states beyond the traditional linear response regime [27].

The paper is organized as follows: In Sec. II we describe the model. The results and discussion thereof are found in Sec. III, with the conclusions drawn in Sec. IV.

II. MODEL

The 2DEG considered in this work is in a lateral square superlattice of quantum dots in a GaAs heterostructure subjected to a perpendicular homogeneous external magnetic field. The effective mass of the electrons is $m^* = 0.067m_e$, the dielectric constant $\kappa = 12.4$, and the effective g -factor is $g^* = -0.44$.

A. The static system

The Hamiltonian of the static 2DEG-cavity system is

$$H = H_e + H_{\text{int}} + H_\gamma, \quad (1)$$

where

$$H_e = H_0 + H_{\text{Zee}} + V_{\text{H}} + V_{\text{per}} + V_{\text{xc}}, \quad (2)$$

describes the 2DEG in a square array of quantum dots and

$$H_0 = \frac{1}{2m^*} \pi^2, \quad \text{with} \quad \pi = \left(\mathbf{p} + \frac{e}{c} \mathbf{A} \right). \quad (3)$$

The external vector potential $\mathbf{A} = (B/2)(-y, x)$ generates the homogeneous magnetic field $\mathbf{B} = B\hat{z}$ perpendicular to the xy -plane of the 2DEG. The spin Zeeman term is $H_{\text{Zee}} = \pm g^* \mu_{\text{B}}^* B/2$, with μ_{B}^* the effective Bohr magneton. The direct Coulomb interaction in terms of the effective local charge density $\Delta n(\mathbf{r}) = n_e(\mathbf{r}) - n_{\text{b}}$ is

$$V_{\text{H}}(\mathbf{r}) = \frac{e^2}{\kappa} \int_{\mathbf{R}^2} d\mathbf{r}' \frac{\Delta n(\mathbf{r}')}{|\mathbf{r} - \mathbf{r}'|}, \quad (4)$$

where $-en_e(\mathbf{r})$ is the electron charge density and $+en_{\text{b}}$ is the homogeneous positive background charge density representing the ionized donors guaranteeing the charge

neutrality of the total system. The square array of quantum dots is represented by the periodic potential

$$V_{\text{per}}(\mathbf{r}) = -V_0 \left[\sin\left(\frac{g_1 x}{2}\right) \sin\left(\frac{g_2 y}{2}\right) \right]^2, \quad (5)$$

where $V_0 = 16.0$ meV. $V_{\text{per}}(\mathbf{r})$ is depicted in Fig. 1 in Ref. [28]. The superlattice is spanned by the spatial vectors $\mathbf{R} = n\mathbf{l}_1 + m\mathbf{l}_2$ with $n, m \in \mathbf{Z}$, where the unit vectors are $\mathbf{l}_1 = L\mathbf{e}_x$ and $\mathbf{l}_2 = L\mathbf{e}_y$, and the reciprocal lattice is spanned by $\mathbf{G} = G_1\mathbf{g}_1 + G_2\mathbf{g}_2$ with $G_1, G_2 \in \mathbf{Z}$ and the unit vectors $\mathbf{g}_1 = 2\pi\mathbf{e}_x/L$ and $\mathbf{g}_2 = 2\pi\mathbf{e}_y/L$. The period of the superlattice is $L = 100$ nm. The Coulomb exchange and correlation potentials V_{xc} of the local spin density approximation (LSDA) are documented in Appendix A of Ref. [29]. The interaction of the 2DEG with the quantized vector potential, \mathbf{A}_γ , of the photon cavity in terms of the electron current, and charge densities is

$$H_{\text{int}} = \frac{1}{c} \int_{\mathbf{R}^2} d\mathbf{r} \mathbf{J}(\mathbf{r}) \cdot \mathbf{A}_\gamma(\mathbf{r}) + \frac{e^2}{2m^*c} \int_{\mathbf{R}^2} d\mathbf{r} n_e(\mathbf{r}) A_\gamma^2(\mathbf{r}). \quad (6)$$

The two terms of the interaction are the para- and the diamagnetic interactions, respectively. In the Appendix of Ref. [26] the electron-photon coupling (6) for a single quantized TE_{011} mode of a cylindrical cavity is derived in the long wavelength approximation, i.e. when the spatial variation of the far-infrared cavity field is small on the scale of L . In terms of the creation and annihilation operators of the eigenstates $|n\rangle$ of the photon number operator, $a_\gamma^\dagger a_\gamma$, the interaction is

$$H_{\text{int}} = g_\gamma \hbar \omega_c \{ l I_x + l I_y \} (a_\gamma^\dagger + a_\gamma) + g_\gamma^2 \hbar \omega_c \mathcal{N} \left\{ \left(a_\gamma^\dagger a_\gamma + \frac{1}{2} \right) + \frac{1}{2} (a_\gamma^\dagger a_\gamma^\dagger + a_\gamma a_\gamma) \right\} \quad (7)$$

with the integrals, I_x , I_y , and \mathcal{N} , that can be interpreted as functionals of the current and the charge densities, respectively, defined in the Appendix of Ref. [26]. The functional interpretation will be essential in understanding the subsequent computational approach. $\omega_c = eB/(m^*c)$ is the cyclotron frequency. It is possible to define a dimensionless coupling strength as

$$g_\gamma = \left\{ \left(\frac{e\mathcal{A}_\gamma}{c} \right) \frac{l}{\hbar} \right\}, \quad (8)$$

where $l = (\hbar c/(eB))^{1/2}$ is the magnetic length, that sets a natural length scale competing with the superlattice length L . The fundamental energy of the photon mode is $E_\gamma = \hbar\omega_\gamma$ and the free photon Hamiltonian is

$$H_\gamma = \hbar\omega_\gamma a_\gamma^\dagger a_\gamma \quad (9)$$

with the zero point energy of the photon mode neglected. In the Appendix of Ref. [26] the vector potential of the

cylindrical TE_{011} cavity photon mode in the long wavelength approximation is derived as

$$\mathbf{A}_\gamma(\mathbf{r}) = \mathbf{e}_\phi \mathcal{A}_\gamma (a_\gamma^\dagger + a_\gamma) \left(\frac{r}{l}\right) \quad (10)$$

with \mathbf{e}_ϕ the unit angular vector in the polar coordinates. This vector potential has the same spatial form as the vector potential \mathbf{A} generating the external homogeneous magnetic field $\mathbf{B} = B\mathbf{e}_z$ [26].

We employ a quantum electrodynamical density functional theory approach, QED-DFT-TP initially presented by Malave [24] and recently adapted to our 2DEG-cavity system by calculating the energy spectrum and the eigenstates of H (1) in a linear functional basis constructed as a tensor product (TP) of the electron and the photon states

$$|\alpha\theta\sigma n\rangle = |\alpha\theta\sigma\rangle \otimes |n\rangle. \quad (11)$$

The photon states $|n\rangle$ are, as stated above, the eigenstates of the photon number operator, and the electron states $|\alpha\theta\sigma\rangle$ are the single-electron states of Ferrari constructed for the periodic 2DEG in an external magnetic field at each point in the first Brillouin zone, i.e. $\theta = (\theta_1, \theta_2) \in [-\pi, \pi] \times [-\pi, \pi]$ [29–33], and $\sigma \in \{\uparrow, \downarrow\}$ is the quantum number for the z -component of the electron spin. All the other quantum numbers of the Ferrari states [30] are combined in α , which can be interpreted as a subband index.

The single-electron states of Ferrari satisfy the commensurability condition for the aforementioned competing length scales in the system, that can be expressed as $BA = BL^2 = pq\Phi_0$ in terms of the quantum of the magnetic flux, $\Phi_0 = hc/e$, and the integers p and q [30–32, 34]. Each Landau-band in the energy spectrum is split into pq subbands. It is possible to express the commensurability condition in different ways [30, 34, 35], but it reflects the fact that spatial translations by superlattice vectors in the external magnetic field gather a Peierls phase and have to be replaced by magnetotranslations. In the Appendix of Ref. [26], it is shown that the electron-photon coupling (6) and the vector potential \mathbf{A}_γ do not break the spatial symmetry of the 2DEG system in the external magnetic field and the periodic quantum dot potential.

B. The dynamic system

The real-time excitation of the 2DEG-cavity system is accomplished by applying a short time-dependent modulation of the electron-photon coupling described by a time-dependent Hamiltonian H_{ext} , in addition to the total Hamiltonian (1),

$$H_{\text{ext}}(t) = F(t) \left[g_\gamma \hbar \omega_c \{lI_x + lI_y\} (a^\dagger + a) + g_\gamma^2 \hbar \omega_c \mathcal{N} \left\{ \left(a^\dagger a + \frac{1}{2} \right) + \frac{1}{2} (a^\dagger a^\dagger + aa) \right\} \right] \quad (12)$$

with

$$F(t) = \left(\frac{V_t}{\hbar \omega_c} \right) (\Gamma t)^2 \exp(-\Gamma t) \cos(\omega_{\text{ext}} t), \quad (13)$$

where ω_{ext} is the frequency of the modulation of the electron-photon interaction. Both, the para- and the diamagnetic interactions become time-dependent. This excitation scheme does not lead to direct mixing of states at different θ -points in the Brillouin zone and enables the use of the Liouville-von Neumann equation for the time-evolution of both spin components of the density operator ρ^θ at each θ

$$i\hbar \partial_t \rho^\theta(t) = [H[\rho^\theta(t)], \rho^\theta(t)] \quad (14)$$

implying that the time-dependent Hamiltonian is a functional of the density operator ρ^θ through the electron charge and current densities, that have to be updated in each iteration within the time-steps of the numerical time integration of Eq. (14). We use the Crank-Nicolson scheme for this as it is advantageous for Hermitian systems [36]. Note that the excitation scheme is in a quantized form regarding the cavity photons and includes all the fundamental photon processes inherent in the electron-photon interaction. Moreover, as the interactions and the excitation do not lead to nonvanishing matrix elements between different θ in the reciprocal space, we can extend the dynamical calculation to a larger state space than was possible for the system in the Hartree or the QEDFT approach where the excitation had a finite wavevector [28, 33]. Here, we have thus a larger contribution from higher order electron-photon processes of various types.

The initial conditions for the density operators at $t = 0$ can be set in the linear basis that results from the diagonalization procedure for the static case $\{|\alpha\theta\sigma\rangle\}$ with the associated wavefunctions $\psi_{\alpha\theta\sigma}(\mathbf{r}) = \langle \mathbf{r} | \alpha\theta\sigma \rangle$, while the states $|\alpha\theta\sigma\rangle$, the Ferrari states, correspond to the wavefunctions $\phi_{\alpha\theta\sigma}(\mathbf{r}) = \langle \mathbf{r} | \alpha\theta\sigma \rangle$. Note specially, the notation used with different brackets: $|\alpha\theta\sigma\rangle$ for the Ferrari states, and $|\alpha\theta\sigma\rangle$ for the Coulomb interacting cavity-photon dressed electron states. If in the $\{|\alpha\theta\sigma\rangle\}$ -basis the initial conditions for the corresponding density operators are the static equilibrium states

$$r_{\alpha\sigma, \beta\sigma'}^\theta(0) = f(E_{\alpha\theta\sigma} - \mu) \delta_{\alpha, \beta} \delta_{\sigma, \sigma'}, \quad (15)$$

where f denotes the equilibrium Fermi distribution, then the initial conditions in the $\{|\alpha\theta\sigma\rangle\}$ can be expressed as

$$\rho^\theta(0) = W^\theta \{r^\theta(0)\} (W^\theta)^\dagger \quad (16)$$

implying that the Liouville-von Neumann equation (14) is solved in the same functional tensor product basis (11) as the Hamiltonian for the static system is diagonalized in, delivering its energy spectrum $E_{\alpha\theta\sigma}$ and chemical potential μ . W^θ is the unitary transformation between the two bases in each point θ of the first Brillouin zone. The

initial density matrix is thus not diagonal for computational convenience and, additionally, the initial excitation promotes off-diagonal elements. The time dependent electron density is calculated as

$$n_\sigma(\mathbf{r}, t) = \frac{1}{(2\pi)^2} \int_{-\pi}^{\pi} d\boldsymbol{\theta} \sum_{\alpha\beta} \phi_{\alpha\theta\sigma}^*(\mathbf{r}) \phi_{\beta\theta\sigma}(\mathbf{r}) \rho_{\alpha\sigma, \beta\sigma}^\theta(t) \quad (17)$$

and the time-dependent average photon number

$$N_\gamma(t) = \frac{1}{(2\pi)^2} \sum_\sigma \int_{-\pi}^{\pi} d\boldsymbol{\theta} \text{Tr} \{ \rho_\sigma^\theta(t) a_\gamma^\dagger a_\gamma \} \quad (18)$$

is conveniently evaluated in the $\{|\boldsymbol{\alpha}\theta\sigma\rangle\}$ -basis. The external magnetic field leads to rotational currents in the system which the excitation pulse modulates, so we calculate the dynamical orbital magnetization to monitor the current oscillations [37, 38]

$$Q_J(t) = \frac{1}{2c\mathcal{A}} \int_{\mathcal{A}} d\mathbf{r} (\mathbf{r} \times \langle \mathbf{J}(\mathbf{r}, t) \rangle) \cdot \mathbf{e}_z, \quad (19)$$

with $\mathcal{A} = L^2$. The time-dependent mean charge current density in the system is

$$\mathbf{J}_i(\mathbf{r}, t) = \frac{-e}{m^*(2\pi)^2} \sum_{\alpha\beta\sigma} \int_{-\pi}^{\pi} d\boldsymbol{\theta} \Re \{ \phi_{\alpha\theta\sigma}^*(\mathbf{r}) \boldsymbol{\pi}_i \phi_{\beta\theta\sigma}(\mathbf{r}) \} \rho_{\beta\theta\sigma, \alpha\theta\sigma}^\theta(t) \quad (20)$$

for the Cartesian components $i = x$ or y . The label J in Q_J is not an integer, but refers to the charge current. As the excitation does not break the initial square symmetry of the superlattice the current and the electron densities retain that periodicity. The spatial operators \mathbf{x} and \mathbf{y} are not periodic so we calculate their mean values and those of their combinations from the dynamical electronic density (17). Even though the mean values of the spatial operators are not shown here, we need them to monitor that the center of mass of the electronic system remains stationary with high accuracy, and in order to monitor the small monopole (breathing), Q_0 , and quadrupole oscillations, Q_2 , of the electron density promoted by the excitation, the superlattice square symmetry, and the Lorentz force [28, 33]. The total energy of the photon-dressed 2DEG is calculated as

$$E_{\text{total}} = \text{Tr} \{ (H[\rho(t)] + H_{\text{ext}}[\rho(t); t]) \rho(t) \} - \frac{1}{2} \int_{\mathbf{R}^2} d\mathbf{r} d\mathbf{r}' \frac{e^2 \Delta n(\mathbf{r}, t) \Delta n(\mathbf{r}', t)}{\kappa |\mathbf{r} - \mathbf{r}'|} - \sum_\sigma \int_{\mathcal{A}} d\mathbf{r} n_\sigma(\mathbf{r}, t) V_{\text{xc}, \sigma}(\mathbf{r}, t) + E_{\text{xc}, \sigma}[n_\sigma(\mathbf{r}, t)], \quad (21)$$

where $n_\uparrow + n_\downarrow = n_e$. $E_{\text{xc}, \sigma}$ are the Coulomb exchange correlation functionals, and $V_{\text{xc}, \sigma}$ the corresponding potentials (see Appendix A in Ref. 29). The second line in Eq. (21) represents a counter term to the double counting of the Coulomb interaction in the first line of the equation. It is common to mean-field and DFT models.

III. RESULTS

In order to build up the understanding of the excitation of the system we start with one electron in each quantum dot of the square superlattice in a cylindrical cavity interacting with the photons of the single TE_{011} mode. Even though only one electron resides in each dot it interacts in the sense of DFT through the charge density with the electrons in the other dots, and the exchange Coulomb interaction leads to a large spin splitting in the finite magnetic field due to the unpaired spin in each dot [26].

A. One electron in a dot, $N_e = 1$, variation of the photon energy E_γ

We start by exploring the effects of the photon energy E_γ on the energy subbands, total energy and mean photon number N_γ . We are not implying that this variation is easy to achieve in experiments, but it gives us valuable insight into the features of the model. The static energy spectrum, showing the width of the subbands, versus E_γ is shown in Fig. 1 with the mean photon number color coded (as is indicated with the colorbar). The lowest subband, below the black curve indicating the chemical potential μ , has a red color signifying a low photon component, i.e. the average number of photons in a quantum dot is much closer to 0, than 1. The orange subband above μ is the first photon replica of the ground state and its color indicates that its mean photon number is close to 1. The third horizontal red narrow subband is the other spin component of the ground state, not occupied. Clearly, the photon replicas have a ‘‘slope’’ that indicates their mean photon number as each photon has the energy E_γ . As the states in each subband are cavity photon-dressed electron states, the mean photon number of a subband does not have to be an integer, especially for strong electron-photon coupling. The width of the lower subbands is small as an electron in them is rather localized in each dot potential. The width of the unoccupied higher energy spin component of the ground state subband is smallest as its ‘‘DFT-interaction’’ through the densities is weak.

Fig. 2 displays the total energy E_{total} (a) and the mean photon number N_γ (b) as functions of the photon energy E_γ . The mean photon number decreases monotonously as the photon energy increases. This is expected for $N_e = 1$, but can be very different for a higher number of electrons in a quantum dot [26].

The total energy in Fig. 2(a) shows a very shallow local minimum at 1.4 meV. Interestingly, this behavior is not found in a QEDFT model with the functional used in [29]. That functional was adapted to a 2DEG in a homogeneous magnetic field from a functional originally proposed by Flick [22] for 3D atomic systems. The functional, a gradient based density functional for the electron-photon interactions, is assembled with an ap-

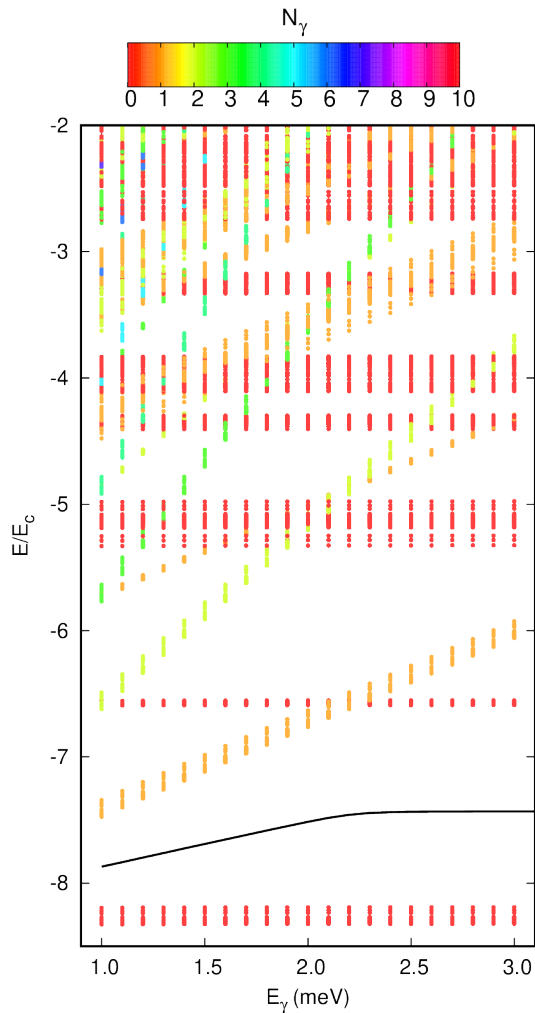


FIG. 1. The width of the energy subbands as a function of the photon energy E_γ . The photon content of the subbands is encoded in the color with red for 0 and violet for 10 photons as the colorbar at the top indicates. The black curve represents the chemical potential μ . $N_e = 1$, $pq = 2$ corresponding to $B = 0.8271$ T or $E_c = \hbar\omega_c = 1.4291$ meV, $g_\gamma = 0.08$, $T = 1.0$ K, and $L = 100$ nm.

proximation which includes all one-photon exchange processes explicitly, while neglecting higher order processes. Of course the self-consistent DFT iterations add effective higher order processes built on these one-photon processes. The QED-DFT-TP approach [24] used here includes multi-photon and higher order processes explicitly. For $E_\gamma < E_c = \hbar\omega_c$ we have a similar monotonic decreasing of E_{total} with increasing photon energy. Looking at the low part of the static energy spectrum in Fig. 1, this is expected, but higher in the energy spectrum of the 2DEG in the quantum dots, the cyclotron energy $\hbar\omega_c$ slowly gains an upper hand in the competition with the confinement energy of the dots. When the photon energy surpasses the cyclotron energy, high order virtual

processes slightly add to the total energy. The shallow local minimum in the total energy is thus a clear indication of the presence of high order virtual photon processes in our model.

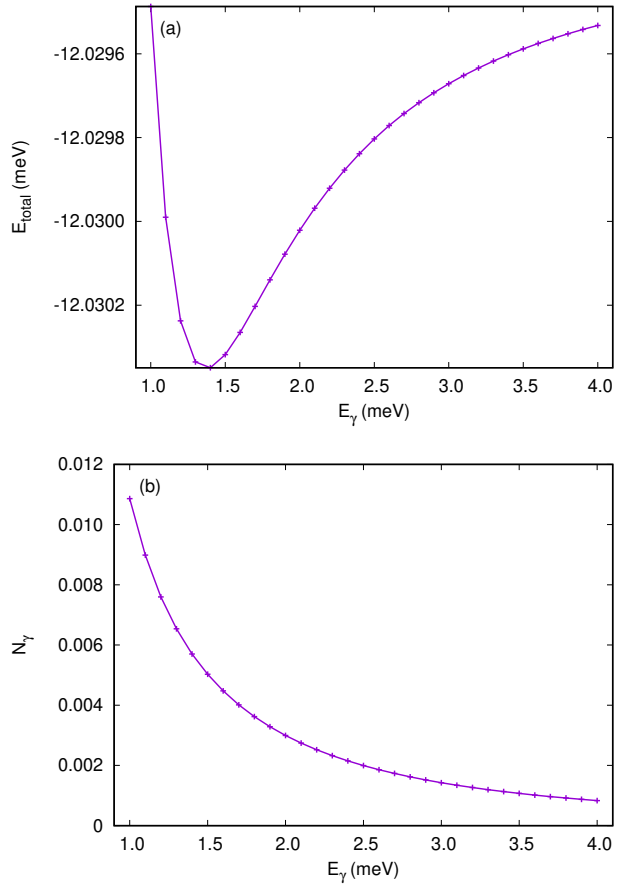


FIG. 2. The total energy E_{total} (a), and the total mean photon number N_γ (b) of the system per unit cell as a function of the photon energy E_γ . $N_e = 1$, $pq = 2$, $T = 1.0$ K, and $L = 100$ nm.

Now we turn our focus on the results of the “real-time” excitation of the system. We use rather strong electron-photon interaction and strong excitation with: $g_\gamma = 0.08$, $V_t/(\hbar\omega_c) = 0.8$, $\hbar\Gamma = 0.5$ meV, and $\hbar\omega_{\text{ext}} = 3.5$ meV. The initial state is the static equilibrium state determined by Eq. (15). The parameter choice will be analyzed below. The time-evolution for the first 30 ps of the total energy E_{total} and the mean photon number N_γ are shown in Fig. 3. The time series are calculated to $t = 100$ ps, but the excitation pulse is cut off at $t = 16$ ps. The results are outside the regime of linear response for a range of photon energy as energy is clearly pumped into the system. After the excitation the mean total energy stays constant, but the photon number oscillates steadily. We analyze the Fourier power spectra for the time series of the variables N_γ and Q_J for the time interval 16 - 100 ps. We present the Fourier power spectra from $\omega/\omega_c = 0$ to 8, or a lower number, without any smoothing or cut-

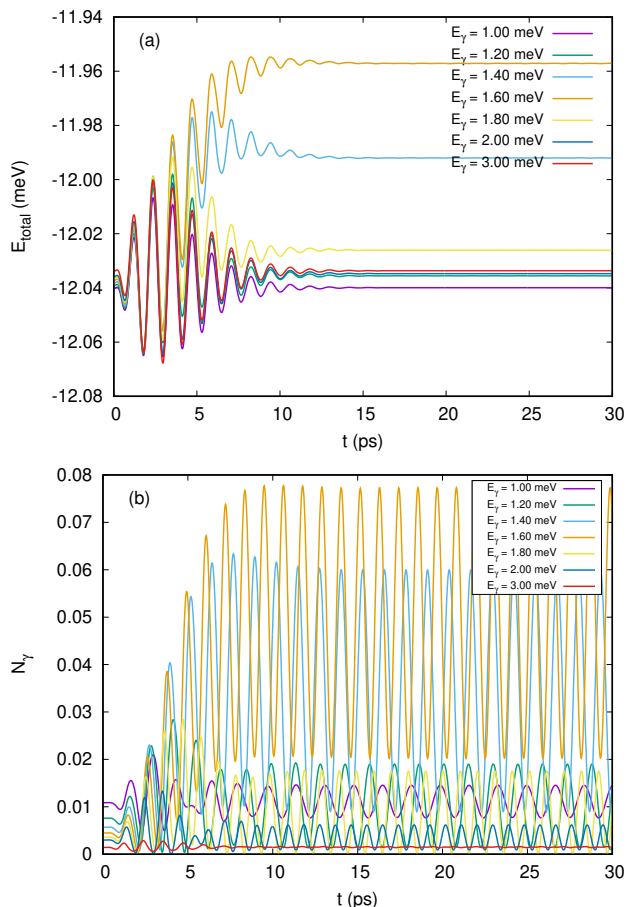


FIG. 3. The time evolution of the total energy E_{total} (a) and the total mean photon number N_γ (b) for the first 30 ps for different values of the photon energy. $g_\gamma = 0.08$, $N_e = 1$, $pq = 2$, $T = 1.0$ K, and $L = 100$ nm. $V_t/(\hbar\omega_c) = 0.8$, $\hbar\Gamma = 0.5$ meV, and $\hbar\omega_{\text{ext}} = 3.5$ meV.

ting off low frequency noise. Since the system is excited slightly into the nonlinear regime we need to analyze the role of the parameters of the excitation pulse.

The Fourier power spectra for the photon number $N_\gamma(\omega)$ is presented in Fig. 4 on a linear (a) and logarithmic scale (b) for selected values of the photon energy E_γ . The location of an excitation peak can be interpreted in terms of the energy of the cavity photons and a shift caused by the electron-photon interactions. The height of the peaks can be related to the parameters of the excitation pulse which has a broad frequency range with a maximum around $\hbar\omega = 3.5$ meV corresponding to $\omega/\omega_c \approx 2.5$, reflecting that $\hbar\omega_{\text{ext}} = 3.5$ meV. At the end of this subsection the parameter choice for the excitation pulse is addressed. In Fig. 4 the excitation peak for $E_\gamma = 1.4$ meV is just above $\omega/\omega_c = 2$, but a glance at the static spectrum in Fig. 1 shows the lowest photon replica with approximately 1 photon is barely over 1.4 meV above the ground state, corresponding to ω/ω_c slightly larger than 1. The excitation has thus mainly a contribution from a 2-photon diamagnetic transition, the

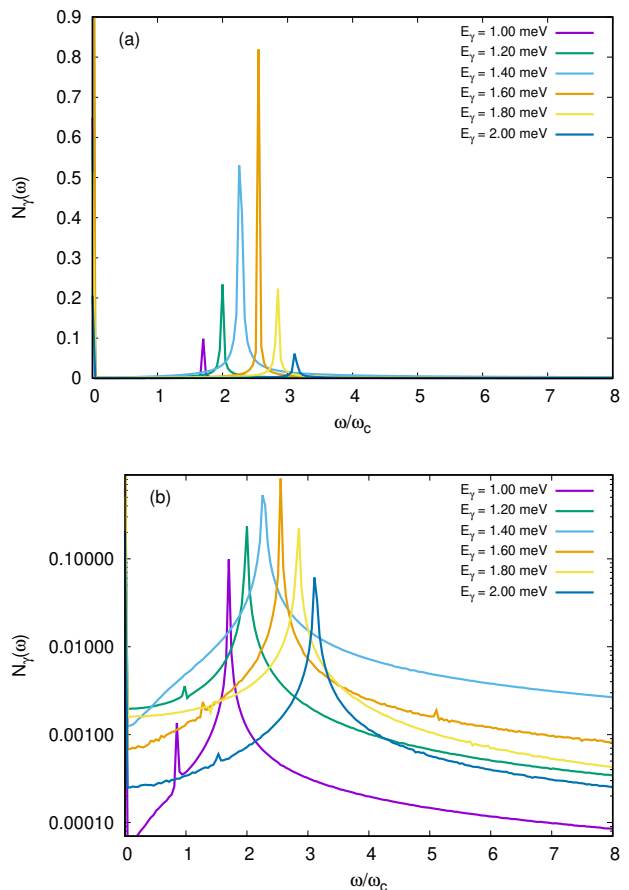


FIG. 4. The Fourier power spectra for the excitation of the total mean photon number N_γ for the system for several values of the photon energy E_γ with a linear (a), or logarithmic scale (b). The Fourier transform is taken after the excitation pulse has vanished. $g_\gamma = 0.08$, $N_e = 1$, $pq = 2$, $T = 1.0$ K, and $L = 100$ nm. $V_t/(\hbar\omega_c) = 0.8$, $\hbar\Gamma = 0.5$ meV, and $\hbar\omega_{\text{ext}} = 3.5$ meV.

second term in Eq. (6), (7), and (12). The dispersion of the excitation peaks with increasing E_γ confirms this idea as the second photon replica in Fig. 1 has a higher slope than the first replica with respect to E_γ . Fig. 4(b) with the logarithmic scale shows weak paramagnetic 1-photon peaks just around or above $\omega/\omega_c = 1$. The diamagnetic e-photon interaction is much stronger than the paramagnetic one in the cylindrical cavity with a TE₀₁₁ mode and a related excitation pulse for the system in an external homogeneous magnetic field, but we need to look closer at this.

Further details emerge as the excitation power spectrum for the dynamic orbital magnetization $Q_J(\omega)$ is viewed in Fig. 5. We confirm that the location of the main peaks of $N_\gamma(\omega)$ and $Q_J(\omega)$ coincide, but $Q_J(\omega)$ displays several smaller peaks besides the main peak. First, we recognize higher order diamagnetic transitions at energies a bit larger than $4E_\gamma$ and $6E_\gamma$, but in addition there are also peaks at energies slightly larger than E_γ ,

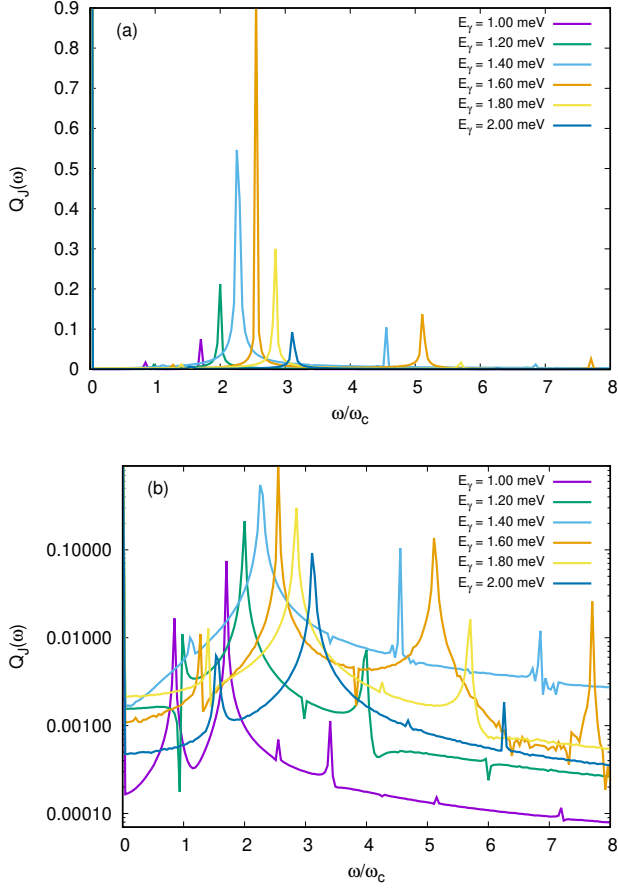


FIG. 5. The Fourier power spectra for the excitation of the mean orbital magnetization Q_J for the system for several values of the photon energy E_γ with a linear (a), or logarithmic scale (b). The Fourier transform is taken after the excitation pulse has vanished. $g_\gamma = 0.08$, $N_e = 1$, $pq = 2$, $T = 1.0$ K, and $L = 100$ nm. $V_t/(\hbar\omega_c) = 0.8$, $\hbar\Gamma = 0.5$ meV, and $\hbar\omega_{\text{ext}} = 3.5$ meV.

$3E_\gamma$, and $5E_\gamma$ that can be identified as paramagnetic transitions.

The excitation pulse induces time-dependent changes in the rotational current distribution of the system, but for one electron in a dot the Lorentz force only leads to small radial charge density (breathing) oscillations in the system. All the same, the energy range offered by the excitation pulse with $\hbar\omega_{\text{ext}} = 3.5$ meV activates strong diamagnetic transitions, virtual and real. In Fig. 6, one can see how a variation of the pulse frequency through the parameter $\hbar\omega_{\text{ext}}$, and its duration through $\hbar\Gamma$, can influence the relative strength of the excitation peaks. The shape of the excitation pulse can be used to tune the relative strength of the pulses representing either mainly the fundamental para- or diamagnetic transitions, or their respective higher harmonics.

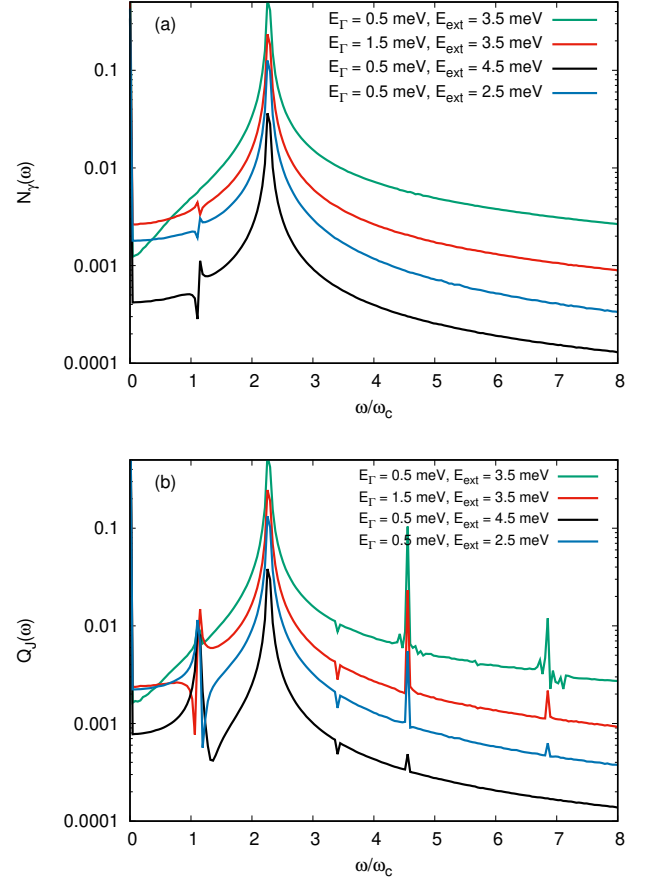


FIG. 6. The Fourier power spectra for the excitation of the mean total photon number N_γ (a) and the mean orbital magnetization Q_J (b) for the system for $E_\gamma = 1.4$ meV. $E_\Gamma = \hbar\Gamma$, and $E_{\text{ext}} = \hbar\omega_{\text{ext}}$. The Fourier transform is taken after the excitation pulse has vanished. $g_\gamma = 0.08$, $N_e = 1$, $pq = 2$, $T = 1.0$ K, and $L = 100$ nm. $V_t/(\hbar\omega_c) = 0.8$.

B. One electron in a dot, $N_e = 1$, variation of the excitation strength V_t

In Subsection III A it became clear that the excitation of the system can take it outside the regime where linear response is appropriate to describe its time evolution. This opens the question how the strength of the excitation influences its response if other parameters are kept constant. Fig. 7 displays the $N_\gamma(\omega)$ excitation peak for different values of the excitation strength V_t . For low values of the excitation strength only one peak is seen but the height of the peaks seems to grow in a slightly superlinear fashion with increasing V_t , but no shift is seen. Both the mean total energy and the mean photon number grow in a similar fashion showing that the system is not in the linear response regime as the excitation strength V_t is increased. For the highest values of V_t a small side peak appears, that reflects the fact that neither the ground state energy subband nor the second photon replica of

it are totally flat in reciprocal space. Like in Subsec-

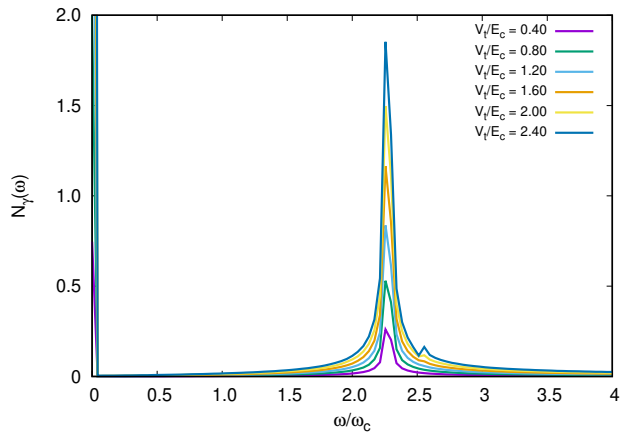


FIG. 7. The Fourier power spectra for the excitation of the total mean photon number N_γ for the system for several values of the excitation strength $V_t/(\hbar\omega_c)$. The Fourier transform is taken after the excitation pulse has vanished. $g_\gamma = 0.08$, $N_e = 1$, $pq = 2$, $T = 1.0$ K, and $L = 100$ nm. $E_\gamma = 1.4$ meV, $\hbar\Gamma = 0.5$ meV, and $\hbar\omega_{\text{ext}} = 3.5$ meV.

tion III A the $Q_J(\omega)$ excitation shows more structure as the excitation strength increases as Fig. 8 shows. Again the diamagnetic excitations are stronger than the paramagnetic ones, and the oscillator strength of the paramagnetic excitations loses relative strength compared to the diamagnetic ones as V_t increases. For the higher diamagnetic peaks more complex structure emerges with stronger V_t . This modified structure can here be correlated to changes of high lying subbands caused by their interactions due to Rabi resonances as is shown in Fig. 9. The figure shows only the energy subbands of the lower in energy spin component. Below the chemical potential is the occupied lowest subband. Above it are the unoccupied first and second photon replicas of the lowest subband, respectively with a simple structure. The third and in particular the fourth photon replica of the ground subband show complex structures resulting from both the effects of the periodic superlattice and the electron-photon interaction. The fourth photon replica determines the excitation peaks seen around $\omega/\omega_c \approx 4.5$. The change of a photon replica subband in reciprocal space modifies the van Hove singularities in its density of states with accompanying possible splitting of excitation peaks [39, 40]. The excitation peaks convey information about the bandstructure of the system.

Complex structures caused by Rabi resonances and the periodicity of the superlattice were seen relatively lower (compared to the chemical potential) in the energy spectrum for a higher number of electrons in a dot in Fig. 5 in Ref. [26].

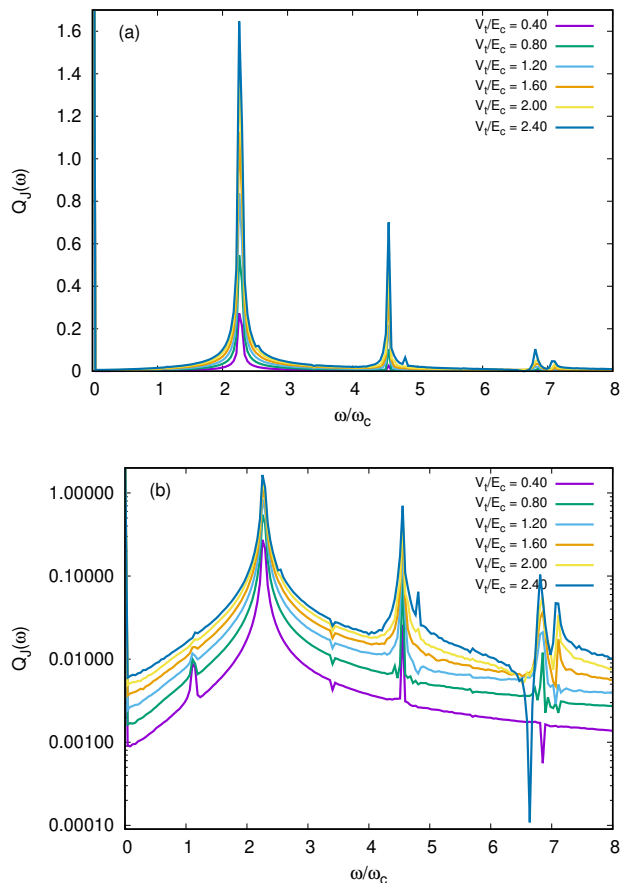


FIG. 8. The Fourier power spectra for the excitation of the mean orbital magnetization Q_J for the system for several values of excitation strength $V_t/(\hbar\omega_c)$ with a linear (a), or logarithmic scale (b). The Fourier transform is taken after the excitation pulse has vanished. $g_\gamma = 0.08$, $N_e = 1$, $pq = 2$, $T = 1.0$ K, and $L = 100$ nm. $E_\gamma = 1.4$ meV, $\hbar\Gamma = 0.5$ meV, and $\hbar\omega_{\text{ext}} = 3.5$ meV.

C. One electron in a dot, $N_e = 1$, variation of the electron-photon coupling strength g_γ

In this subsection we explore how the excitation spectra change when the electron-photon interaction strength g_γ is varied. The influence of g_γ can be expected to be complex as it enters the system through two different types of interactions to different order.

The first 30 ps of the time evolution of the total energy of the system are seen in Fig. 10. For the lower values of g_γ the system is clearly not in the linear response regime, but for the highest 3 values it is very close to it. The photon energy is here $E_\gamma = 1.40$ meV and as was shown in Subsection III A the parameter choice for the excitation pulse lead to finite energy to be pumped into the system. As the coupling is increased the processes active in the system are lifted above the energy regime in which the excitation pulse easily supplies energy to it.

The static energy spectrum as a function of g_γ is dis-

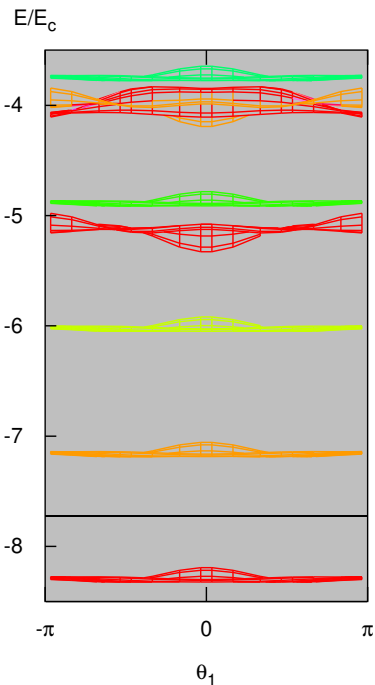


FIG. 9. The energy bandstructure of only the lower in energy spin component projected on the θ_1 direction in the 1st Brillouin zone for $N_e = 1$, and $pq = 2$. The color of the bands indicates their photon content with red for 0 and violet for 10. The chemical potential μ is shown by the horizontal black line. $E_c = \hbar\omega_c = 1.4291$ meV, $g_\gamma = 0.08$, $T = 1.0$ K, $L = 100$ nm, and $E_\gamma = 1.4$ meV.

played in Fig. 11. We note that none of the subbands is horizontal as even the occupied ground state acquires a small photon component that grows with increasing coupling. The electron-photon coupling determines the character of the emerging quasi-particle states, the cavity-photon dressed electron states.

Fig. 12 presents the excitation spectra for the different values of g_γ on a linear (a) and a logarithmic (b) scale. The photon energy is $E_\gamma = 1.4$ meV. The height of the excitation peaks could not have been easily guessed without a calculation, as it neither strictly follows the amount of energy pumped into the system nor a simple function of the dimensionless coupling g_γ or the total energy of the system. The reasons for this have to be partially sought in the static energy spectrum in Fig. 11. The structure of the subbands in the energy spectrum above $E/E_c \approx -5$ is extremely complex regarding crossings, anticrossings, and photon content, and can not be easily demonstrated by the band widths. It is even difficult to resolve it clearly with surface plots in reciprocal space, but this behavior hides Rabi resonances for both parts of the electron-photon interactions, that strongly modify higher order virtual and real processes. The location of the peaks, or the distance between them, is not linear with respect to g_γ but clearly demonstrates an additional g_γ^2 -component, indicating that simple pertur-

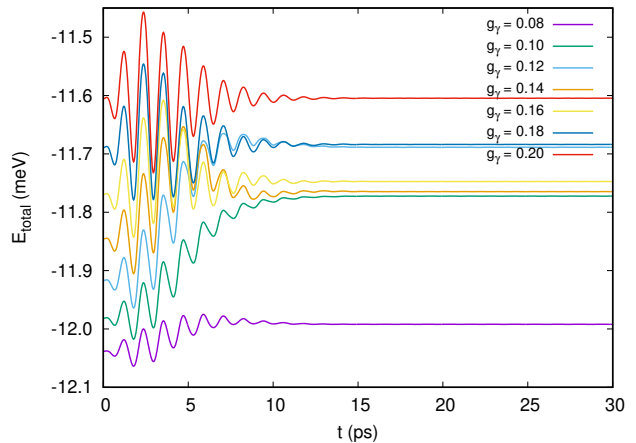


FIG. 10. The time evolution of the total energy for the first 30 ps for different values of the dimensionless electron-photon coupling g_γ . $E_\gamma = 1.4$ meV, $N_e = 1$, $pq = 2$, $T = 1.0$ K, and $L = 100$ nm. $V_t/(\hbar\omega_c) = 0.8$, $\hbar\Gamma = 0.5$ meV, and $\hbar\omega_{\text{ext}} = 3.5$ meV.

bational ideas may not always be sufficient to identify the nature of the virtual and real processes that contribute to the peaks, though the main contribution can be clear in some cases.

Further higher order and paramagnetically active excitations are seen in the excitation spectra for $Q_J(\omega)$ shown in Fig. 13. The second order diamagnetic excitation peaks are slightly spread in energy (or ω) compared to the first order ones. This reflects properties of the static energy spectrum in Fig. 11, where it is seen that the higher photon replicas tend to have a higher slope with respect to g_γ than the lower ones.

D. More than 1 electron in a dot, $N_e > 1$

In this subsection we explore the excitation of system with 2 and 3 electrons at the low magnetic field $B = 0.4135$ T corresponding to $E_c = \hbar\omega_c = 0.7145$ meV, and the number of magnetic flux quanta $pq = 1$ through the unit cell of the square lattice. The photon energy is chosen to be $E_\gamma = 1.0$ meV corresponding to the ratio $E_\gamma/E_c \approx 1.4$.

The excitation spectrum for $N_e = 2$ is shown in Fig. 14. In this case no photon replica is occupied initially and the two electrons are in a singlet spin state without an enhanced spin splitting. For the lower coupling $g_\gamma = 0.01$ the overlapping peaks close to $\omega/\omega_c = 1.4$ have a main contribution from a one photon paramagnetic transition. The corresponding peaks close to $\omega/\omega_c = 2.8$ are much lower and can be assigned to a two photon diamagnetic transition. The diamagnetic peaks for $g_\gamma = 0.01$ are very small as $g_\gamma^2 \ll g_\gamma$. This size ratio for the diamagnetic and the paramagnetic excitation peaks turns around for the strong coupling $g_\gamma = 0.08$ and the peaks get blue-shifted away from the simple ratios of $E_\gamma/E_c \approx 1.4$ or 2.8

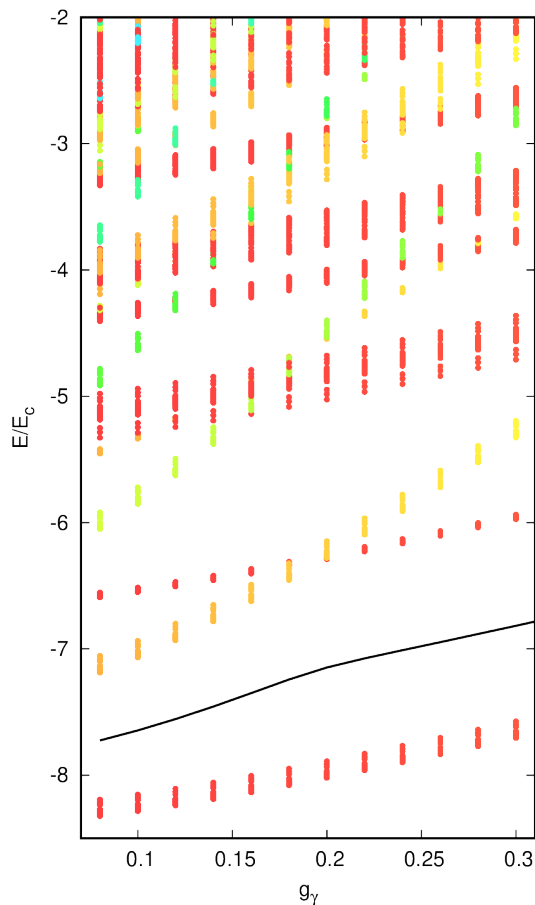


FIG. 11. The width of the energy subbands as a function of the dimensionless electron-photon coupling g_γ . The photon content of the subbands is encoded in the color with red for 0 and violet for 10 photons. The black curve represents the chemical potential μ . $E_\gamma = 1.4$ meV, $pq = 2$ corresponding to $B = 0.8271$ T or $E_c = \hbar\omega_c = 1.4291$ meV, $N_e = 1$, $T = 1.0$ K, and $L = 100$ nm.

when higher order interaction effects start to contribute to them as the electron-photon coupling is increased.

Similar behavior for the excitation spectra can be seen for the case of 3 electrons in a quantum dot presented in Fig. 15. Here all parameters are the same as for the case of two electrons in a dot, but now one photon replica is occupied and the Coulomb exchange interaction leads to a large spin splitting with approximately one unpaired spin. Like, seen earlier in two different approaches for the static calculations, the large spin splitting is slightly reduced by the strong electron-photon interaction for $g_\gamma = 0.08$ [26, 29]. The electron-photon coupling tends to reduce the Coulomb exchange interaction.

For both the cases of 2 and 3 electrons in a quantum dot presented here, the excitation does not add much energy to the systems for the chosen parameters. It remains very close to the linear response regime. The increased half-width of the excitation peaks compared to

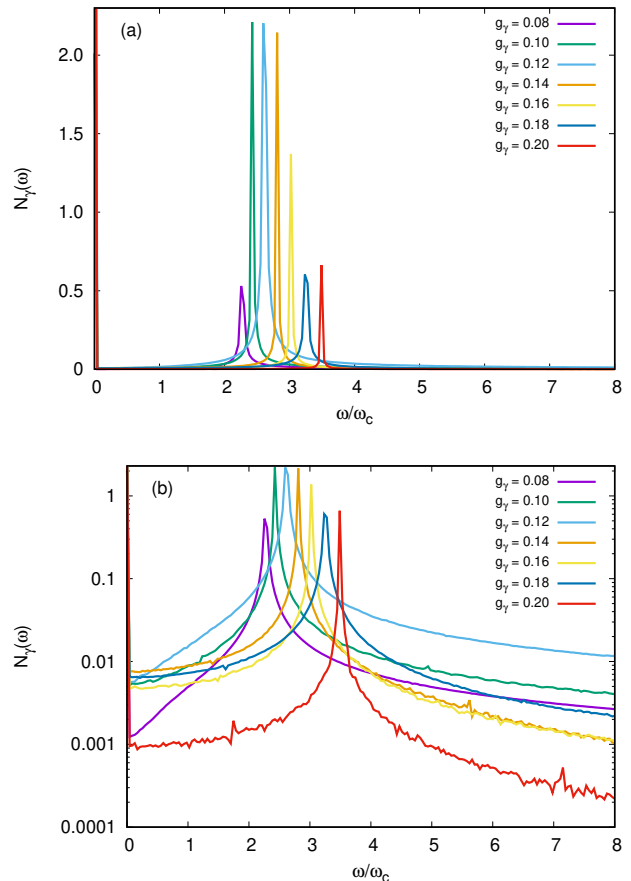


FIG. 12. The Fourier power spectra for the excitation of the total mean photon number N_γ for the system for several values of the dimensionless electron-photon coupling g_γ with a linear (a), or logarithmic scale (b). The Fourier transform is taken after the excitation pulse has vanished. $E_\gamma = 1.4$ meV, $N_e = 1$, $pq = 2$, $T = 1.0$ K, and $L = 100$ nm. $V_t/(\hbar\omega_c) = 0.8$, $\hbar\Gamma = 0.5$ meV, and $\hbar\omega_{\text{ext}} = 3.5$ meV.

the $pq = 2$ results in the previous subsections is due to the smaller cyclotron energy $\hbar\omega_c$ and the increased width of the energy subbands at the lower magnetic field, where the electrons in the dots are more influenced by electrons in the neighboring dots in the square lattice.

We have performed calculations for a higher number of electrons in a quantum dot. For a low cavity photon energy resulting in more photon replicas to be occupied initially, the number of iterations in each time step tends to grow and it can take unreasonable CPU-time to gather enough time points for accurate Fourier transforms. This reminds us that the effective electron-photon coupling strength is not only set by the single parameter g_γ .

IV. CONCLUSIONS

We use a DFT-QED-TP approach for the Coulomb interacting electrons of a 2DEG in a square array of quan-

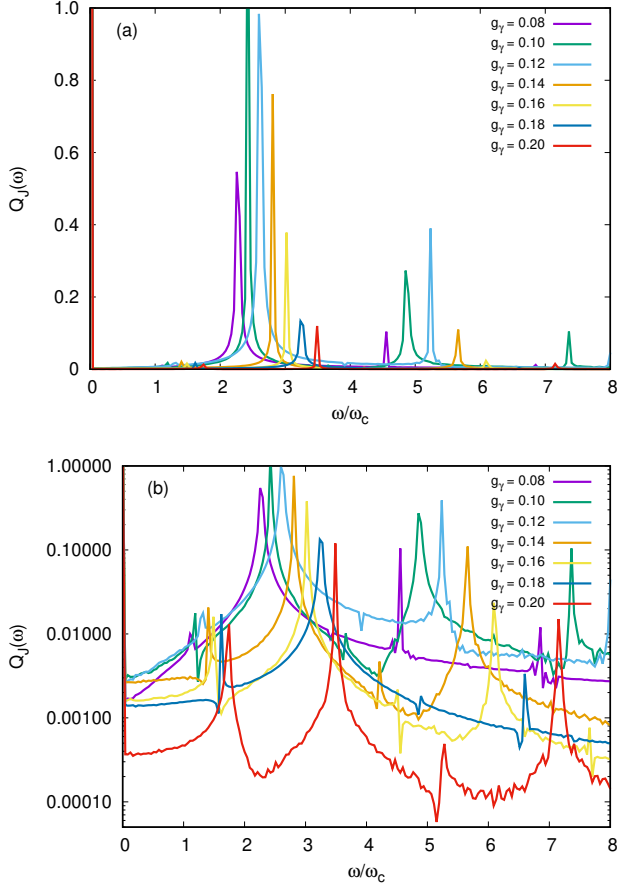


FIG. 13. The Fourier power spectra for the excitation of the dynamical orbital magnetization Q_J for the system for several values of the dimensionless electron-photon coupling g_γ with a linear (a), or logarithmic scale (b). The Fourier transform is taken after the excitation pulse has vanished. $E_\gamma = 1.4$ meV, $N_e = 1$, $pq = 2$, $T = 1.0$ K, and $L = 100$ nm. $V_t/(\hbar\omega_c) = 0.8$, $\hbar\Gamma = 0.5$ meV, and $\hbar\omega_{\text{ext}} = 3.5$ meV.

tum dots in a homogeneous external perpendicular magnetic field. The 2DEG is placed in a circular cylindrical FIR photon cavity supporting one TE_{011} mode. The coupling of the 2DEG to the cavity photons is described by a configuration interaction approach that is updated in each DFT iteration in both the static case, and in each time step of the dynamical evolution of the system after a short excitation.

The vector potential for the external magnetic field, and the cavity vector potential in the long wavelength approximation have the same spatial form. The electron-photon coupling includes both the para- and the diamagnetic interaction parts, and the quantized excitation pulse conforms to the symmetry of the cavity and includes both types of the electron-photon interaction. These choices for the cavity and the excitation allow us to tailor the excitation to steer the relative strength of resonances that can either be assigned to para- or diamagnetic electron-photon coupling. It is, for example, possi-

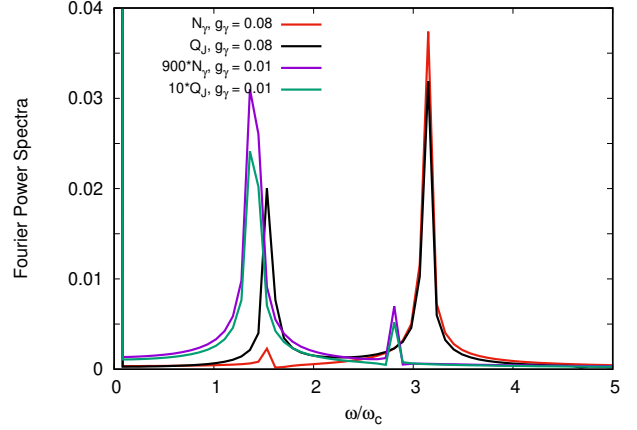


FIG. 14. The Fourier power spectra for the excitation of the total mean photon number N_γ and the dynamic orbital magnetization Q_J for the system for two values of the dimensionless electron-photon coupling g_γ . The Fourier transform is taken after the excitation pulse has vanished. $E_\gamma = 1.0$ meV, $N_e = 2$, $pq = 1$, $T = 1.0$ K, and $L = 100$ nm. $V_t/(\hbar\omega_c) = 0.8$, $\hbar\Gamma = 0.5$ meV, $\hbar\omega_{\text{ext}} = 3.5$ meV, and $E_c = \hbar\omega_c = 0.7145$ meV.

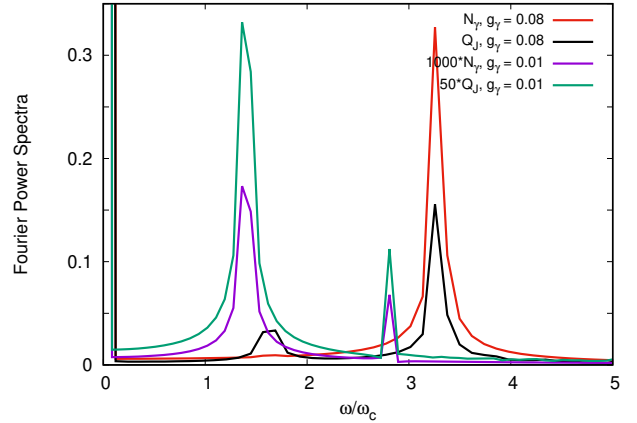


FIG. 15. The Fourier power spectra for the excitation of the total mean photon number N_γ and the dynamic orbital magnetization Q_J for the system for two values of the dimensionless electron-photon coupling g_γ . The Fourier transform is taken after the excitation pulse has vanished. $E_\gamma = 1.0$ meV, $N_e = 3$, $pq = 1$, $T = 1.0$ K, and $L = 100$ nm. $V_t/(\hbar\omega_c) = 0.8$, $\hbar\Gamma = 0.5$ meV, $\hbar\omega_{\text{ext}} = 3.5$ meV, and $E_c = \hbar\omega_c = 0.7145$ meV.

ble to excite almost exclusively diamagnetic processes in the system.

The cylindrical photon cavity and the form of the excitation promote magnetic dipole and higher order magnetic processes in the system. The same is true about the effects of the cylindrical cavity on the static system. The underlying reason for the effectiveness of this is the fact that the system is in an external homogeneous magnetic field.

The real-time approach to the excitation allows us to choose parameters to go beyond a simple linear response regime. Energy can be pumped into the system and non-linear higher order processes can be activated leading to higher order harmonics of the fundamental processes, and blue shifting of resonances due to high order virtual and real processes.

This particular excitation mode of the 2DEG does not lead to center of mass oscillations of the electron system in each dot like a conventional FIR electrical dipole excitation is known to do, but is closely related to methods used for measurements of the cyclotron resonance. Both the original and the generalized Kohn theorem are broken. The obtained excitation spectra reveal information about the subband structure in the array of coupled quantum dots with special emphasis on the photon replica subbands, or generally the photon content of the subbands.

Changes to the structure of individual photon replica subbands due to their interactions through Rabi resonances and the influences of the square superlattice lead to changes in the van Hove singularities in their density of states. The difference in the density of states singularities of two photon replica subbands with active transitions between them exposes the singularities as splittings of excitation peaks in the respective excitation spectra. For the case of one electron in each quantum dot this happens due to Rabi resonances in high lying subbands that start to contribute to the excitation process as its strength is increased. For a higher number of electrons in a dot this regime is expected to happen for a lower excitation strength.

As the electron number in each dot is increased, weak quadrupole and monopole (breathing) excitation modes for the charge density can be seen appearing in the time dependent induced density. The monopole oscillations are connected with the rotational current oscillation through the Lorentz force, but the quadrupole modes arise due to the square symmetry of the superlattice.

It is important to be aware of that sometimes in our analysis we tend to use concepts to explain occurring phenomena in terms of perturbation theory, even though the results show us that this view has its limits as we are dealing with a model that is solved iteratively self-consistently for all the interactions, the Coulomb-interaction, and the electron-photon interaction. The QED-DFT-TP approach gives us a methodology to access physical phenomena in a nonperturbative regime of

an extended solid state electron systems in a photon cavity. The purity, or the mobility, and the polarizability of a 2DEG in a GaAs heterostructure make it an ideal system to explore these phenomena.

ACKNOWLEDGMENTS

This work was financially supported by the Research Fund of the University of Iceland grant No. 92199, and the Icelandic Infrastructure Fund for “Icelandic Research e-Infrastructure (IREI)”. The computations were performed on resources provided by the Icelandic High Performance Computing Center at the University of Iceland. V. Mughnetsyan and V. Gudmundsson acknowledge support by the Higher Education and Science Committee of Armenia (grant No. 21SCG-1C012). V. Gudmundsson acknowledges support for his visit to the National Taiwan University from the National Science and Technology Council, Taiwan under Grants No. NSTC 113-2811-M-002-001 and No. NSTC 112-2119-M-002-014.

H.-S. Goan acknowledges support from the National Science and Technology Council, Taiwan under Grants No. NSTC 112-2119-M-002-014, No. NSTC 111-2119-M-002-007, and No. NSTC 111-2627-M-002-001, and from the National Taiwan University under Grants No. NTU-CC-112L893404 and No. NTU-CC-113L891604. H.-S. Goan is also grateful for the support from the “Center for Advanced Computing and Imaging in Biomedicine (NTU-112L900702)” through The Featured Areas Research Center Program within the framework of the Higher Education Sprout Project by the Ministry of Education (MOE), Taiwan, and the support from the Physics Division, National Center for Theoretical Sciences, Taiwan.

J.-D. Chai acknowledges support from the National Science and Technology Council, Taiwan under Grants No. NSTC113-2112-M-002-032 and No. MOST110-2112-M-002-045-MY3. J.-D. Chai is also grateful for the support from the Physics Division, National Center for Theoretical Sciences, Taiwan.

C.-S. Tang acknowledges funding support by the National United University through Contract No. 113-NUUPRJ-01.

V. Moldoveanu acknowledges financial support from the Core Program of the National Institute of Materials Physics, granted by the Romanian Ministry of Research, Innovation and Digitalization under the Project PC2-PN23080202.

-
- [1] T. Ando, A. B. Fowler, and F. Stern, Electronic properties of two-dimensional systems, *Rev. Mod. Phys.* **54**, 437–672 (1982).
- [2] E. Batke, D. Heitmann, and C. W. Tu, Plasmon and magnetoplasmon excitation in two-dimensional electron space-charge layers on GaAs, *Phys. Rev. B* **34**, 6951–6960 (1986).
- [3] T. Demel, D. Heitmann, P. Grambow, and K. Ploog, Far-infrared response of one-dimensional electronic systems in single- and two-layered quantum wires, *Phys. Rev. B* **38**, 12732–12735 (1988).
- [4] D. Liu and S. Das Sarma, Quantum theory of infrared

- absorption in a grating-coupled two-dimensional electron gas, *Phys. Rev. B* **44**, 9122–9125 (1991).
- [5] R. Krahn, M. Hochgräfe, C. Heyn, and D. Heitmann, Bernstein modes in density-modulated two-dimensional electron systems and quantum dots, *Phys. Rev. B* **61**, R16319–R16322 (2000).
- [6] W. Kohn, Cyclotron Resonance and de Haas-van Alphen Oscillations of an Interacting Electron Gas, *Phys. Rev.* **123**, 1242–1244 (1961).
- [7] P. Bakshi, D. A. Broido, and K. Kempa, Electromagnetic response of quantum dots, *Phys. Rev. B* **42**, 7416–7419 (1990).
- [8] P. A. Maksym and T. Chakraborty, Quantum dots in a magnetic field: Role of electron-electron interactions, *Phys. Rev. Lett.* **65**, 108–111 (1990).
- [9] V. Gudmundsson and R. R. Gerhardtts, Self-consistent model of magnetoplasmons in quantum dots with nearly parabolic confinement potentials, *Phys. Rev. B* **43**, 12098–12101 (1991).
- [10] V. Gudmundsson, A. Brataas, P. Grambow, B. Meurer, T. Kurth, and D. Heitmann, Bernstein modes in quantum wires and dots, *Phys. Rev. B* **51**, 17744–17754 (1995).
- [11] K. Bollweg, T. Kurth, D. Heitmann, V. Gudmundsson, E. Vasiliadou, P. Grambow, and K. Eberl, Detection of Compressible and Incompressible States in Quantum Dots and Antidots by Far-Infrared Spectroscopy, *Phys. Rev. Lett.* **76**, 2774–2777 (1996).
- [12] T. Darnhofer, M. Suhrke, and U. Rössler, Far-infrared response of quantum dots: filling factor dependence at high magnetic fields, *EPL (Europhysics Letters)* **35**, 591 (1996).
- [13] C. Dahl, B. Jusserand, A. Izrael, J. Gérard, L. Ferlazzo, and B. Etienne, Plasmons in the modulated and confined 2DEG: A Raman scattering study, *Superlattices and Microstructures* **15**, 441–445 (1994).
- [14] C. Steinebach, C. Schüller, and D. Heitmann, Resonant Raman scattering of quantum dots, *Phys. Rev. B* **59**, 10240–10245 (1999).
- [15] T. Maag, A. Bayer, S. Baierl, M. Hohenleutner, T. Korn, C. Schüller, D. Schuh, D. Bougeard, C. Lange, R. Huber, M. Mootz, J. E. Sipe, S. W. Koch, and M. Kira, Coherent cyclotron motion beyond Kohn’s theorem, *Nature Physics* **12**, 119–123 (2016).
- [16] E. A. Henriksen, P. Cadden-Zimansky, Z. Jiang, Z. Q. Li, L.-C. Tung, M. E. Schwartz, M. Takita, Y.-J. Wang, P. Kim, and H. L. Stormer, Interaction-Induced Shift of the Cyclotron Resonance of Graphene Using Infrared Spectroscopy, *Phys. Rev. Lett.* **104**, 067404 (2010).
- [17] S. Smolka, W. Wuester, F. Haupt, S. Faelt, W. Wegscheider, and A. Imamoglu, Cavity quantum electrodynamics with many-body states of a two-dimensional electron gas, *Science* **346**, 332–335 (2014).
- [18] Q. Zhang, M. Lou, X. Li, J. L. Reno, W. Pan, J. D. Watson, M. J. Manfra, and J. Kono, Collective non-perturbative coupling of 2D electrons with high-quality-factor terahertz cavity photons, *Nature Physics* **12**, 1005 (2016).
- [19] M. Ruggenthaler, J. Flick, C. Pellegrini, H. Appel, I. V. Tokatly, and A. Rubio, Quantum-electrodynamical density-functional theory: Bridging quantum optics and electronic-structure theory, *Phys. Rev. A* **90**, 012508 (2014).
- [20] J. Flick, M. Ruggenthaler, H. Appel, and A. Rubio, Kohn & Sham approach to quantum electrodynamical density-functional theory: Exact time-dependent effective potentials in real space, *Proceedings of the National Academy of Sciences* **112**, 15285–15290 (2015).
- [21] N. Tancogne-Dejean, M. J. T. Oliveira, X. Andrade, H. Appel, C. H. Borca, G. Le Breton, F. Buchholz, A. Castro, S. Corni, A. A. Correa, U. De Giovannini, A. Delgado, F. G. Eich, J. Flick, G. Gil, A. Gomez, N. Helbig, H. Hübener, R. Jestädt, J. Jornet-Somoza, A. H. Larsen, I. V. Lebedeva, M. Lüders, M. A. L. Marques, S. T. Ohlmann, S. Pipolo, M. Rampp, C. A. Rozzi, D. A. Strubbe, S. A. Sato, C. Schäfer, I. Theophilou, A. Welden, and A. Rubio, Octopus, a computational framework for exploring light-driven phenomena and quantum dynamics in extended and finite systems, *The Journal of Chemical Physics* **152** (2020), 124119.
- [22] J. Flick, Simple Exchange-Correlation Energy Functionals for Strongly Coupled Light-Matter Systems Based on the Fluctuation-Dissipation Theorem, *Phys. Rev. Lett.* **129**, 143201 (2022).
- [23] J. Flick, H. Appel, M. Ruggenthaler, and A. Rubio, Cavity Born–Oppenheimer Approximation for Correlated Electron–Nuclear-Photon Systems, *Journal of Chemical Theory and Computation* **13**, 1616–1625 (2017).
- [24] J. Malave, A. Ahrens, D. Pitagora, C. Covington, and K. Varga, Real-space, real-time approach to quantum-electrodynamical time-dependent density functional theory, *The Journal of Chemical Physics* **157** (2022), 194106.
- [25] F. Schlawin, D. M. Kennes, and M. A. Sentef, Cavity quantum materials, *Applied Physics Reviews* **9**, 011312 (2022).
- [26] V. Gudmundsson, V. Mughnetsyan, H.-S. Goan, J.-D. Chai, N. R. Abdullah, C.-S. Tang, V. Moldoveanu, and A. Manolescu, Magneto-optical properties of a quantum dot array interacting with a far-infrared photon mode of a cylindrical cavity, *Phys. Rev. B* **109**, 235306 (2024).
- [27] R. Kubo, Statistical-Mechanical Theory of Irreversible Processes. I. General Theory and Simple Applications to Magnetic and Conduction Problems, *J. Phys. Soc. Japan* **12**, 570 (1957).
- [28] V. Gudmundsson, V. Mughnetsyan, N. R. Abdullah, C.-S. Tang, V. Moldoveanu, and A. Manolescu, Controlling the excitation spectrum of a quantum dot array with a photon cavity, *Phys. Rev. B* **108**, 115306 (2023).
- [29] V. Gudmundsson, V. Mughnetsyan, N. R. Abdullah, C.-S. Tang, V. Moldoveanu, and A. Manolescu, Effects of a far-infrared photon cavity field on the magnetization of a square quantum dot array, *Phys. Rev. B* **106**, 115308 (2022).
- [30] R. Ferrari, Two-dimensional electrons in a strong magnetic field: A basis for single-particle states, *Phys. Rev. B* **42**, 4598 (1990).
- [31] H. Silberbauer, Magnetic minibands in lateral semiconductor superlattice, *J. Phys. C* **4**, 7355 (1992).
- [32] V. Gudmundsson and R. R. Gerhardtts, Effects of screening on the Hofstadter butterfly, *Phys. Rev. B* **52**, 16744 (1995).
- [33] V. Gudmundsson, V. Mughnetsyan, N. R. Abdullah, C.-S. Tang, V. Moldoveanu, and A. Manolescu, Unified approach to cyclotron and plasmon resonances in a periodic two-dimensional GaAs electron gas hosting the Hofstadter butterfly, *Phys. Rev. B* **105**, 155302 (2022).
- [34] R. D. Hofstadter, Energy levels and wave functions of Bloch electrons in rational and irrational magnetic fields, *Phys. Rev. B* **14**, 2239 (1976).

- [35] J. Herzog-Arbeitman, A. Chew, and B. A. Bernevig, Magnetic Bloch theorem and reentrant flat bands in twisted bilayer graphene at 2π flux, *Phys. Rev. B* **106**, 085140 (2022).
- [36] J. Crank and P. Nicolson, A practical method for numerical evaluation of solutions of partial differential equations of the heat-conduction type, *Mathematical Proceedings of the Cambridge Philosophical Society* **43**, 50–67 (1947).
- [37] J. Desbois, S. Ouvry, and C. Texier, Persistent currents and magnetization in two-dimensional magnetic quantum systems, *Nuclear Physics B* **528**, 727–745 (1998).
- [38] V. Gudmundsson, S. I. Erlingsson, and A. Manolescu, Magnetization in short-period mesoscopic electron systems, *Phys. Rev. B* **61**, 4835–4843 (2000).
- [39] D. Weiss, K. v. Klitzing, K. Ploog, and G. Weimann, Landau level broadening and Van Hove singularities in lateral surface superlattices, *Surf. Sci.* **229**, 88 (1990).
- [40] L. Van Hove, The Occurrence of Singularities in the Elastic Frequency Distribution of a Crystal, *Phys. Rev.* **89**, 1189–1193 (1953).